




Aluminum-doped zinc oxide thickness controllable wavelengths in visible light and high responsivity devices using interrupted flow atomic layer deposition

Po-Hsien Tseng¹, Yu-Sheng Lai^{2,*}, Cheng-Ming Huang², Shang-Yu Tsai¹, and Fu-Hsiang Ko^{1,*} 

¹ Department of Materials Science and Engineering, National Yang Ming Chiao Tung University, Hsinchu 300, Taiwan

² Taiwan Semiconductor Research Institute, Hsinchu 300, Taiwan

Received: 8 March 2024

Accepted: 28 April 2024

Published online:

8 May 2024

© The Author(s), 2024

ABSTRACT

In this study, we develop a highly sensitive visible light photodetector that utilizes a thin-film structure composed of low-cost aluminum-doped zinc oxide (AZO) and n-type silicon. The AZO thickness can be adequately controlled to fit the different wavelengths of interest for photodetectors in the visible light range using interrupted flow atomic layer deposition (ALD). This in situ aluminum doping method ensures a uniform aluminum distribution within the AZO thin films and effectively increases the internal film reflections and photoresponsivity. The Schottky interface with n-type silicon is created by degenerated AZO due to the lower Fermi level, and visible light can effectively penetrate the underlying depletion zone. Optical simulation of the high conductivity of AZO indicated that the optimal thickness was 54.6, 65.8, and 91.7 nm for devices illuminated with 450 nm blue, 525 nm green and 700 nm red light, respectively. Hall effect measurements confirmed that the AZO film can achieve a low resistivity of $5 \times 10^{-4} \Omega\text{-cm}$ and high carrier concentration of $3 \times 10^{20} \text{ cm}^{-3}$ at a suitable precursor ratio. Additionally, AZO films offer multifunctionality by providing optical antireflective properties and forming Schottky junctions with n-type silicon to enable photoelectric conversion. This multifunctional role of AZO was experimentally validated through electrical, optical, and optical-to-electrical experiments, which showed that the optimized device can reach an optical responsivity of approximately 10.7 AW^{-1} at specific visible light wavelengths. The significant photoelectrical conversion efficiency and simple thin-film structure design facilitate future applications in light intensity measurement, such as in colorimetry or fluorometry.

Address correspondence to E-mail: yslai@narlabs.org.tw; fhko@nycu.edu.tw

1 Introduction

Within the context of contemporary technological advancements, sensors play a critical role in automation systems, facilitating the acquisition of environmental parameters and their subsequent conversion into electrical signals. The semiconductor device places significant emphasis on the research and development of sensors, constituting a pivotal dimension in technological progress. Extensive exploration of sensor technologies, such as thermal [1, 2], gas [3, 4], pressure [5, 6], and optical sensors [7, 8] has been reported. Notably, photodetectors have emerged as a focal point in current mainstream research, garnering substantial interest owing to their versatile utility and energy-efficient attributes. In biomedicine, photodetectors play a significant role in optical imaging and diagnosis, offering noninvasive benefits. Photodetectors are also integrated into fiber optic communication systems for communication purposes. They convert optical signals into electrical signals to enable high-speed and long-distance data transmission. The versatility of photodetectors underscores their irreplaceable role in modern society and their potential to drive future technique innovations [9, 10].

A visible light sensor is a specialized photodetector for detecting specific light bands, which is useful for systems that require single-wavelength detection. The integration of a visible light sensor typically includes microlenses, color filters, light pipes, metal wire layers, photodetector arrays, and accompanying electrical circuit items [11]. This integration makes circuit assembly complex and limits miniaturization. The majority of photodetectors are conventional p–n junctions that are simpler to fabricate than photodetectors at Schottky junctions. However, p–n junctions have slower operating speeds because of the minority carrier storage effect as device switching is poorly suited for detecting rapid changes in light signals.

In the realm of advanced sensor technologies, graphene-based photodetectors have garnered increased amounts of attention due to their unique properties. These devices, which are known for their high speed, sensitivity, and bandwidth, operate across a broad spectrum range, making them versatile for various applications, including high-speed communications and biomedical imaging. The high electron mobility of graphene enables these detectors to achieve rapid response times, which is crucial for quick optical signal detection [12–14]. However, despite their potential,

graphene-based photodetectors face challenges in optical optimization due to the low optical absorption efficiency of graphene, which is attributed to its monolayer structure. While certain studies employ substrates to craft nanostructures that can enhance the optical properties of these devices, achieving significant efficiency [15, 16], the intricate nature of these structures poses challenges. These issues complicate cost reduction efforts and integration with existing semiconductor manufacturing processes.

In the conventional metal–semiconductor Schottky junction, incident light traverses the metal layer to reach the junction depletion region, which is different from the conventional p–n junction wherein light must navigate a thick neutral region. Nonetheless, the conventional Schottky junction presents a challenge in facilitating effective absorption of incident light by the semiconductor, which is primarily attributable to the heightened reflectivity and absorption characteristics inherent in the metallic device. This is a significant impediment in optical performance and manifest as limitations in achieving optimal photoelectrical responses.

The proposed methodology entails the utilization of a nanohole array positioned on a thin metal film to address the previously described challenges [17]. This strategy optimizes device dimensions by capitalizing on the surface plasmon resonance inherent in the metal and the optical cavity interference phenomena. Consequently, this configuration selectively permits the passage of a defined spectral band for addressing these issues. While the metal in this method serves the triple function of an electrode, a filter, and a Schottky junction former, endowing the metal hole array with good transmittance for specific wavelength, its sensitivity remains suboptimal due to the elevated refractive coefficient and extinction coefficient of the metal. Moreover, the implementation of a nanohole array through precise lithography technology increases the overall complexity and cost of the process. Many studies have focused on utilizing active devices, such as bipolar junction transistors (BJTs) or field-effect transistors (FETs), which amplify electrical signals to enhance photoelectric signal output, thereby achieving superior light sensitivity. However, such active devices require additional power for biasing, conflicting with the increasing emphasis on green energy solutions. Consequently, this investigation seeks to devise a light detector design that operates without bias voltage, aligns with green energy principles, and

is being simple, cost-effective, and highly sensitive. Additionally, if the optical properties can be adjusted across any visible light spectrum, this technology could synergize with other green energy systems, such as photocatalysis for dye degradation [18–23]. In scenarios where dye concentrations are minimal, the system should exhibit heightened sensitivity to swiftly detect low dye concentrations. Moreover, a visible light sensor with enhanced sensitivity could be pivotal in monitoring hydrogen gas leaks within hydrogen storage systems [24]. Notably the junction-based photosensor operates without any voltage bias, underscoring its status as a green energy device.

Zinc oxide (ZnO) is a promising material for transparent electrodes [25–27] due to its potential applications in photoelectric and piezoelectric devices [28–31]. Despite its many advantageous properties, the high resistivity of ZnO limits its effectiveness as a conducting electrode. To enhance the conductivity of ZnO-based electrodes, Group III elements such as aluminum, gallium, or indium are often doped into ZnO [32–36]. For example, aluminum-doped zinc oxide (AZO) is a popular transparent conductive metal oxide with higher conductivity than ZnO [37–40]. In addition to the electrical properties of the AZO material, the low refractive index and near-zero extinction coefficient of AZO under visible light make it an excellent transparent electrode. Compared to indium tin oxide (ITO), which is a more commonly researched and mature transparent conductive electrode material, AZO does not require expensive or toxic metal elements [41]. Furthermore, the AZO material has better thermal stability and visible light transparency, making it more suitable for high-power, long-term use in light detectors. Various methods such as sputtering [42], sol–gel methods [43], chemical vapor deposition [44], and atomic layer deposition (ALD) have been used to prepare AZO films. The conventional oxide diffusion method for doping ZnO through ALD involves growing a layer of Al_2O_3 on a multilayer ZnO thin film in advance. The aluminum then diffuses into the ZnO via post-annealing at relatively high process temperatures. Additionally, this method requires multiple ZnO layers to dilute the aluminum concentration, which affects the ability to control the thickness of the AZO film and results in a nonuniform distribution of aluminum in the overall AZO film [45]. Compared to the oxide diffusion method, the in situ ALD doping method can control the uniform dopant concentration in the AZO film.

In this study, a new visible light sensor design using a heavily doped AZO thin film as a multifunctional material is proposed. The AZO films are fabricated by interrupted flow ALD with precise thickness control, enabling natural color filtering through thin-film interference. The AZO films also serve as transparent electrodes and Schottky junction formers with n-type silicon, simplifying the device structure and enhancing the photoelectric conversion efficiency. This study adopts a simple film stack structure that requires only one fabrication process and achieves an ultrahigh responsivity of 10.7 AW^{-1} at specific wavelengths. Optical simulation revealed the optimal thickness of the AZO film for different visible light wavelengths of interest.

2 Materials and methods

2.1 Thin-film material

In this study, AZO films were prepared through an ALD system with an interrupted flow method, which is different from the conventional continuous flow method typically utilized in ALD systems. In the ALD process with the continuous flow method, the precursor is grown during flow, which potentially hinders the complete reaction of the precursor. The interrupted flow method incorporates an additional soaking time, allowing the precursor to fully exploit the self-limiting effect. This ALD method contributes to superior film uniformity and crystallinity.

The in situ doping method is employed in this study. The process is described as follows: During the ALD deposition of the ZnO layer on a silicon wafer, the aluminum precursor undergoes simultaneous injection into the chamber. Due to the disparity in binding energies among zinc, aluminum, and oxygen, aluminum supplies zinc, resulting in the formation of n-type-doped AZO. The fabrication sequence of the in situ doping method is presented as follows: The first precursor, DI water, is introduced into the reaction chamber within 50 ms and allowed to soak for 2s without pumping. Subsequently, the residual precursor is purged from the chamber using N_2 gas within 3s, followed by pumping for 8s. Next, the second precursor, diethylzinc (DEZ), is introduced into the reaction chamber within 50 ms and soaked for 2s without pumping. Then, the third precursor, trimethylaluminum (TMA), is introduced into the

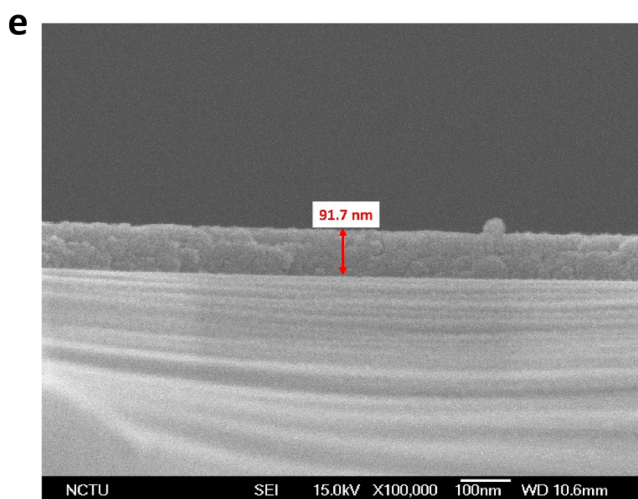
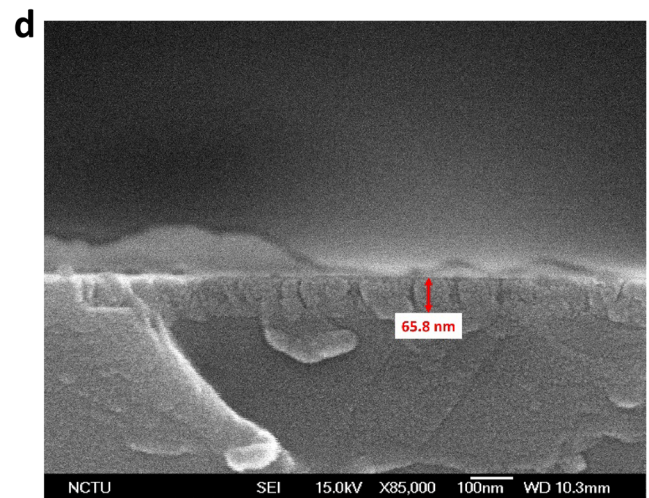
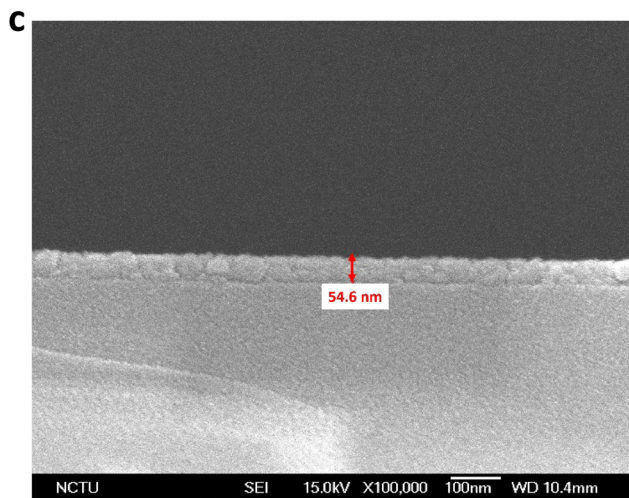
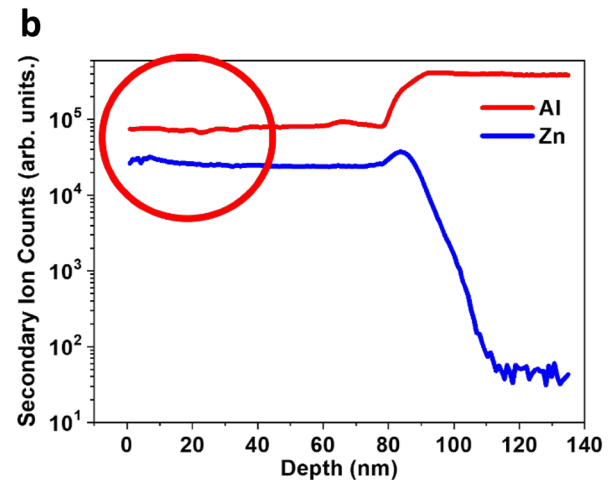
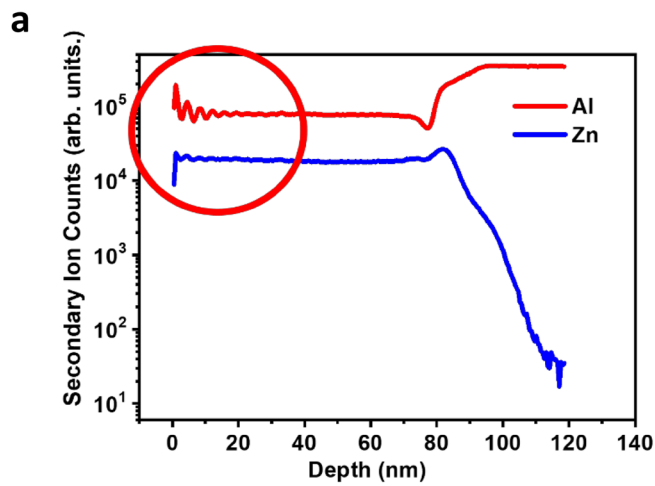


Fig. 1 Depth profile of Al and Zn atoms from secondary ion mass spectrometry (SIMS) and cross-sectional scanning electron microscopy (SEM) images of AZO thin films under different growth conditions. **a** Layered ZnO film and Al₂O₃ film subjected to diffusion annealing treatment; **b** AZO film after interrupted flow and in situ doping method ALD; **c** AZO thickness of 54.6 nm in the SEM image; **d** SEM image of AZO with a thickness of 65.8 nm; and **e** AZO thickness of 91.7 nm in the SEM image

reaction chamber within 10 ms to displace some of the original lattice sites of Zn. Afterward, the residual precursor is purged from the chamber using N₂ gas within 8 s and pumped out within 10 s. This method exhibits enhanced effectiveness in doping compared to conventional oxide diffusion method, enabling a more uniform aluminum distribution within fewer ZnO layers, which is crucial for the precise adjustment of AZO film thickness. The uniformity of the aluminum distribution in the AZO films produced via in situ doping, in contrast to those prepared via conventional methods, was confirmed through secondary ion mass spectrometry (SIMS) analysis, as illustrated in Fig. 1a–b. The superior uniformity of AZO doped by the in situ doping method is advantageous for the stringent control of optical properties and thickness modulation in optical sensors. In contrast to the conventional thermal diffusion method, which involves a layered ZnO and Al₂O₃ structure followed by high-temperature annealing to induce aluminum diffusion, this method results in nonuniform doping in the range of 20 nm (as illustrated in Fig. 1a) on the surface. In contrast, the in situ doping method from interrupted flow ALD (Fig. 1b) ensures a more homogeneous atom distribution for minimizing light scattering at interfaces and enhancing the performance of optical devices. The precursor for Zn in this work was diethylzinc (DEZ), and the precursor for Al was trimethylaluminum (TMA). These precursors were purchased from PentaPro Materials.

2.2 Optical simulation

Various thicknesses of ZnO films from ALD were characterized by ellipsometry, and the ellipsometry model used in this work was an Ellipsometer M2000. The refractive index and extinction coefficient of the AZO film can be determined from the visible light spectra. Prior to the ALD experiment on the AZO film, optical simulation was achieved using the Macleod optical thin-film simulation software. The simulation is

beneficial choosing the optimal AZO thickness that contributes to the lowest surface reflection and best light absorption for red, green, and blue visible light.

2.3 Device fabrication and photoelectric characterization

The fabrication of the device begins with a thorough RCA cleaning process for the n-Si wafer surface. Following cleaning, TiN is deposited on the n-Si back side via the PVD, acting as a back electrode. In situ Al doping of ZnO occurs at reaction temperature of 250 °C. The desired thickness of AZO is subsequently deposited to attain the optimal thickness at blue, green, and red wavelengths. A UV–Vis spectrometer is used to measure and confirm the optical properties of the fabricated devices via the optical simulation. The spectrometer used in this work was Hitachi UH5700 instrument. The I–V curve of the device was measured in a dark room to determine the Schottky junction of the device. The ammeter mode was used to measure the photoelectric current on–off curve of the device under illumination. This approach ensures that the signal originates solely from the light-to-electric signal and that the photoelectric current output of the device can be accurately observed.

In this study, the light sources included blue (450 nm), green (525 nm), and red (700 nm) LED lights with an intensity of 65 μWcm⁻². The device area is 1 cm × 1 cm and the light spot encompasses the entire device. All electrical measurements were conducted using a Keithley 2400 instrument. The tool has a theoretical measurement limit of one pA for current and 100 nV for voltage, meeting the signal requirements for the photoelectric signals.

3 Results and discussion

3.1 Design of the AZO thin film

The in situ doping method employed in this research demonstrates superior efficacy in doping compared to the conventional oxide diffusion approach, facilitating a more homogeneous distribution of aluminum across fewer ZnO layers. This homogeneity is vital for the precise calibration of AZO film thickness. Unlike conventional methods, the uniformity of the aluminum distribution within AZO films produced via in situ doping was validated through secondary

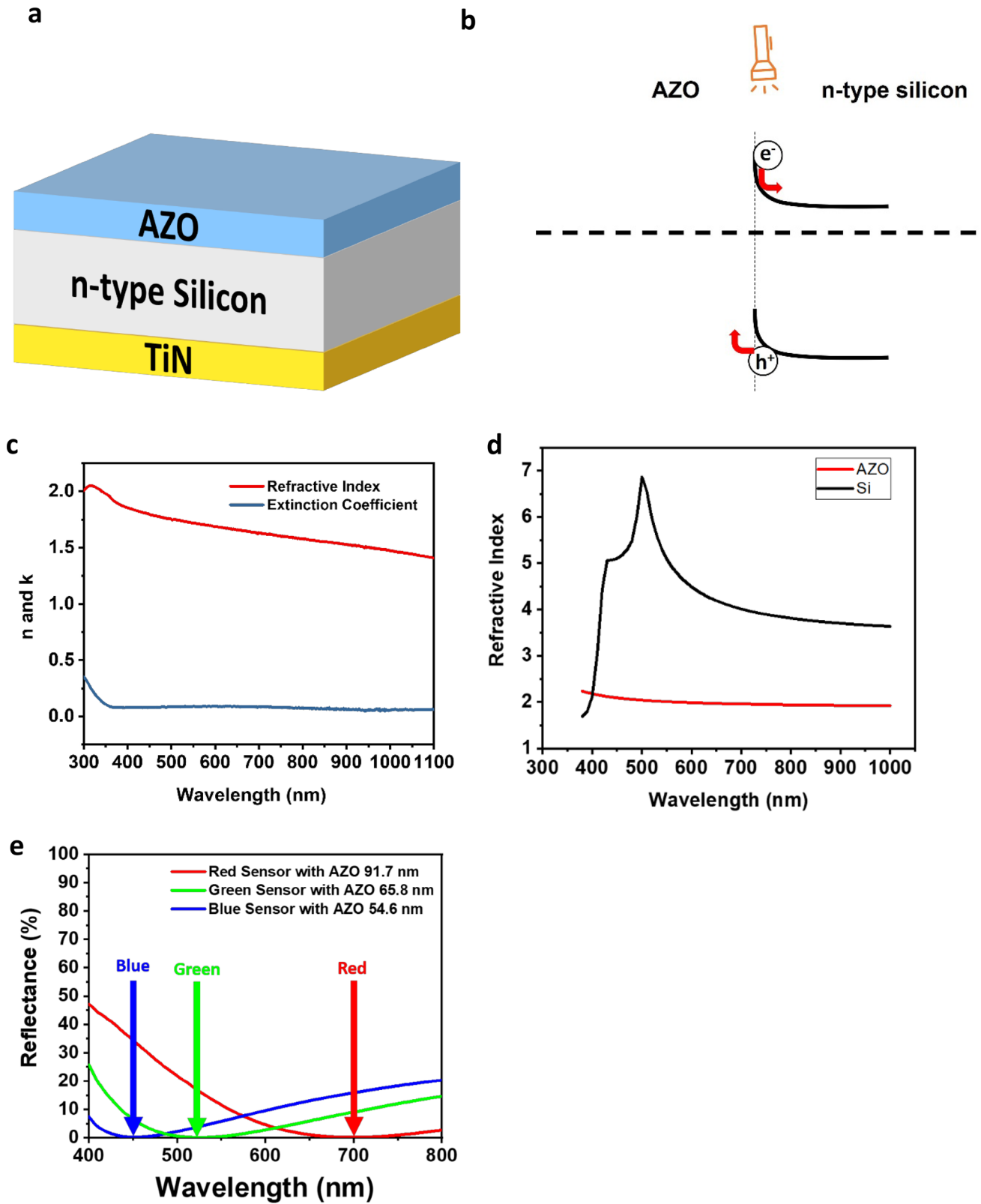


Fig. 2 **a** Device structure for an AZO film Schottky junction with an n-type Si and TiN film as the back electrode; **b** band diagram of AZO and an n-type silicon Schottky junction; **c** refractive index (n) and extinction coefficient (k) for the obtained AZO film from in situ-doped interrupted flow ALD; **d** refractive coefficient (n) for the AZO and Si materials; **e** surface reflectance spectra of the AZO device from the interrupted flow and in situ-doped ALD films with thicknesses of 54.6, 65.8, and 91.7 nm obtained from a UV–vis spectrometer

ion mass spectrometry (SIMS) analysis, as depicted in Fig. 1. This enhanced uniformity, attributed to the in situ doping approach, is beneficial for the meticulous regulation of optical properties and thickness modulation in optical sensors. Diverging from the traditional thermal diffusion technique, which involves a stratified ZnO and Al₂O₃ structure followed by high-temperature annealing to foster aluminum diffusion—leading to uneven doping within the top most 20 nm (as illustrated in Fig. 1a)—the in situ doping method via interrupted flow atomic layer deposition (ALD) (shown in Fig. 1b) guarantees a more uniform atomic distribution. This uniformity is crucial for reducing light scattering at interfaces, thereby boosting the performance of optical devices. Moreover, the in situ doping technique requires a lesser quantity of aluminum atoms for doping, subsequently necessitating a reduced amount of ZnO film to counterbalance the aluminum atoms. This aspect is particularly advantageous for the stringent regulation of the AZO film thickness. SEM cross-sectional images of three distinct AZO thicknesses in visible light detectors, established in this study—Fig. 1c (54.6 nm), Fig. 1d (65.8 nm), and Fig. 1e (91.7 nm)—demonstrate consistency with the predetermined thicknesses. This consistency underscores the ability of the ALD with interrupted flow and in situ doping methods to cultivate high-quality films at precise thicknesses that are fully aligned with the requirements of optical devices.

The design structure of the visible light sensor is illustrated in Fig. 2a. An AZO film with the optimal thickness is deposited on the surface of n-type Si, and TiN film is obtained as the ohmic contact metal electrode for the back electrode. Figure 2b shows the band diagrams of AZO and n-type silicon. In this study, AZO, with a doping concentration of 10^{20} , qualifies as a degenerate semiconductor, effectively rendering it a metallized material. Conversely, the n-type silicon utilized possesses a doping concentration of 10^{15} , which leads to the formation of a Schottky junction

between AZO and n-type silicon with the depletion region exclusively situated on the silicon surface. According to the band diagram depicted in Fig. 2b, upon the absorption of light by silicon, which results in the generation of electron–hole pairs, electrons and holes migrate toward silicon in the conduction band and toward AZO in the valence band, respectively. Under closed-circuit conditions, this process culminates in the generation of an effective photoelectric current, which is denoted as the short-circuit current (I_{sc}). Conversely, in an open-circuit scenario, the system yields a photoelectric voltage output, which is referred to as the open-circuit voltage (V_{oc}).

The optical properties of AZO are crucial for designing simple AZO thin films of different thicknesses rather than optical nanostructures for visible light sensors. The optical properties of the refractive coefficient n and extinction coefficient k for AZO film are shown in Fig. 2c. The obtained refractive coefficient of the AZO film is approximately 1.5 to 2 under visible light. In contrast, the extinction coefficient of the AZO film is almost zero in the visible wavelength range. These observations confirm the low reflection and high transmission properties of the AZO film in the visible light region.

Figure 2c compares the refractive coefficient n of the AZO film and silicon substrate in the visible light range. Compared with the n value of 4–5 for silicon, the 1.5–2 refractive coefficient of the AZO film is better for the interface with the refractive coefficient of air. The optical properties of AZO can effectively reduce the optical reflection of visible light sensors and achieve high optical absorption according to the thin-film interference principle. Because of the very low extinction coefficient of AZO, increasing the thickness of AZO film in the visible range did not alter the optical absorption of the film. This phenomenon is beneficial for light absorption in the ultrashallow light region at the silicon interface for direct enhancement of photoelectric conversion. Notably, the refractive index of silicon abruptly increases in the blue light band, as shown in Fig. 2d. This often leads to a substantial increase in the light reflectivity of silicon-based photodetector devices within the blue band. Hence, the sensitivity of photodetectors can be affected by blue light. As shown in Fig. 2c, AZO exhibited a low refractive index and near-zero extinction coefficient in the blue light band. By maintaining strict control over the thickness of the AZO film to fulfill thin-film interference conditions, a state of zero reflection can be achieved,

which allows for high transmission, thereby enabling silicon to exhibit high absorption. Notably, the AZO thin film permits the nearly unimpeded transmission of light, enabling it to directly impinge upon the silicon surface, precisely at the depletion zone. The band diagram presented in Fig. 2b elucidates that the electron-hole pairs, engendered by the absorption of light within the depletion zone, can be effectively segregated by the built-in electric field, thereby generating an electrical signal. This phenomenon underscores the notion that light absorption is only consequential within the depletion zone. The architectural design

employed in this study optimizes the conditions such that light is not only intensely focused but also effectively absorbed by the depletion zone, culminating in the efficient generation of an electrical signal. This enhancement increases the sensitivity of the silicon-based photodetector. Figure 2d shows the UV-visible light spectra measured by three distinct visible light sensors. Each sensor demonstrates an optical reflection of 0% within its respective detection band. These findings confirm when the thickness of the AZO film is well controlled, the device can exhibit exceptional optical absorption for a specific band. Consequently,

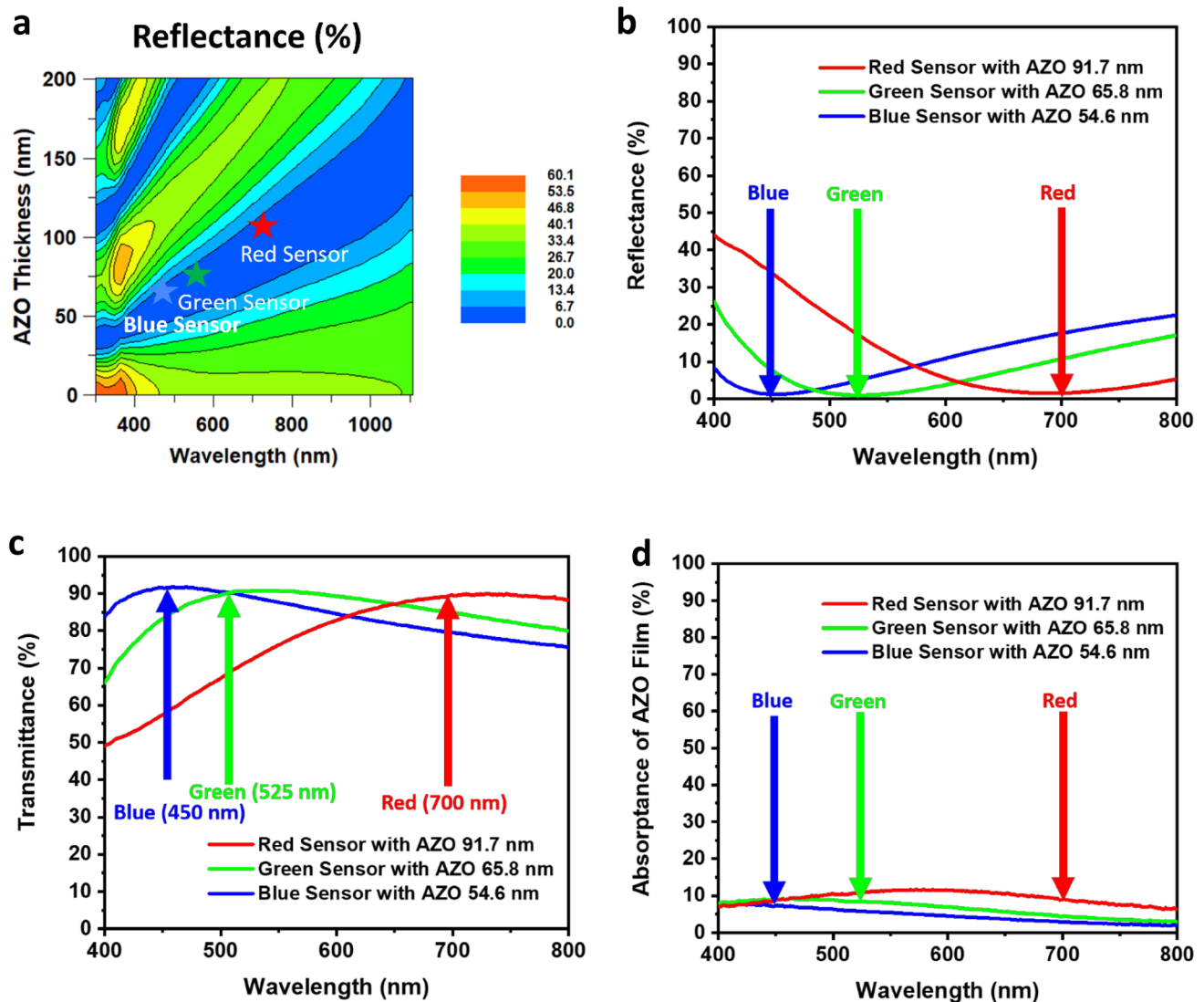


Fig. 3 Optical simulation plot for the AZO film obtained with Macleod optical thin-film simulation software: **a** Reflectance of the AZO film in various color regions under different light wavelengths and AZO thicknesses from simulation; **b** reflection spec-

tra of different thicknesses of AZO film from simulation; **c** transmittance spectrum of different thicknesses of the AZO film from the simulation; and **d** absorbance spectra of different thicknesses of the AZO film from the simulation

it is anticipated that a device will demonstrate superior sensitivity within this band. The ability of ALD to control film thickness enables precise control of the thickness of high-quality AZO films.

Optical simulation of the AZO film shown in Fig. 3a revealed zero reflection regions in the visible light range of 300–800 nm. These thickness and wavelength intervals are also chosen as the sensor regions. The regions of the sensors in Fig. 3a designed to detect visible light in the blue, green, and red spectra are indicated by star marks in corresponding colors. The simulation results also demonstrate the ability of the created visible light sensors to detect different wavelengths with specific AZO film thicknesses. In other words, optimal optical performance at a given wavelength can be achieved when the sensor thickness meets the sensor area shown in Fig. 3a, at which point the visible light sensor has the highest sensitivity to this wavelength. Figure 3b shows the simulated reflection spectrum of the AZO film between 400 and 800 nm. This optical reflectance behavior from the simulation for AZO film is similar to that of the experiment film, as shown in Fig. 2e. Other optical properties for transmittance and absorptance from simulation are illustrated in Fig. 3c–d. We depict the respective color regions for the red light (700 nm), green light (525 nm), and blue light (450 nm) bands in Fig. 3b–d. The optical simulation clearly suggests that red, green, and blue sensing capabilities can be achieved by deposition of the AZO film by ALD at thicknesses of 91.7, 65.8, and 54.6 nm, respectively. In addition, the AZO films exhibited high transmittance (larger than 90%) of blue, green, and red light at wavelengths of 450, 525, and 700 nm, respectively, as shown in Fig. 3c. Moreover, Fig. 3d shows that the absorptance of the AZO film is very low (lower than 10%). The results of low reflection, low absorption, and high transmittance for the AZO film reveal the effectiveness of our precise design of the AZO thickness for visible light sensors. Consequently, when the light detection device, featuring an optimally calibrated AZO film thickness, is subjected to illumination, the light traverses the AZO film with very little loss or reflection. This process enables the light to directly reach the n-type silicon surface, which is the depletion region of the AZO/n-type silicon Schottky junction. Here, silicon efficiently absorbs light, facilitating the generation of electron–hole pairs. These pairs are subsequently segregated by the built-in electric field within the depletion region, resulting in the formation of effective electrical signals. Hence, it

is anticipated that the light detector will exhibit heightened sensitivity toward specific light wavelengths.

3.2 Photoelectronic performance of the visible light sensor

The I–V curves in Fig. 4a demonstrate similar behavior for bias frequencies between -1 and 1 V in the dark. This observation confirms that all three blue, green, and red light devices can form an effective Schottky junction between the AZO film and the n-type Si substrate. The current repeatability of the turn-on and turn-off properties of the device under dark or different light illuminations (red/700 nm, green/525 nm, and blue/450 nm) is illustrated in Fig. 4b–d. The periodic turn-on current is obtained at a light illumination of $65 \mu\text{Wcm}^{-2}$ light reaches $\sim 7 \times 10^{-4}$ A for red, green, and blue light. This observation suggests that the thickness of the device sensor with AZO thicknesses of 91.7, 65.8, and 54.6 nm can provide excellent photoelectric conversion efficiency.

Figure 4e illustrates the responsivities of the three devices corresponding to their respective optimal detection light bands mentioned in Fig. 2e. Their responsivities can reach 10.7 AW^{-1} at their respective detection wavelengths. This responsivity is approximately two orders of magnitude greater than that of previously reported metal nanopore array detectors ($0.15 \sim 0.35 \text{ AW}^{-1}$). According to the optical simulation result shown in Fig. 3, the thickness of the AZO thin film only needs to be changed to achieve an excellent responsivity of 10.7 AW^{-1} for visible light in the design of the visible light sensor. The high device responsivity is attributed to the transparent AZO conducting electrode with better conductivity, very good antireflection capability at specific wavelengths, and shallow surface of the silicon. Owing to the minimal attenuation of incident visible light by AZO and the meticulous regulation of the AZO film thickness, which yields exceptionally low reflectivity, a substantial portion of the light can directly impinge on the surface of n-type silicon, which is the depletion zone within the AZO/n-type silicon Schottky junction. This interaction facilitates the efficient generation and separation of electron–hole pairs by the built-in electric field, thereby contributing to the high photosensitivity observed. Figure 4f provides various publications on the surface maximum responsivity for different device designs, and our device design has the best photoelectric conversion efficiency and responsivity [17, 46–53].

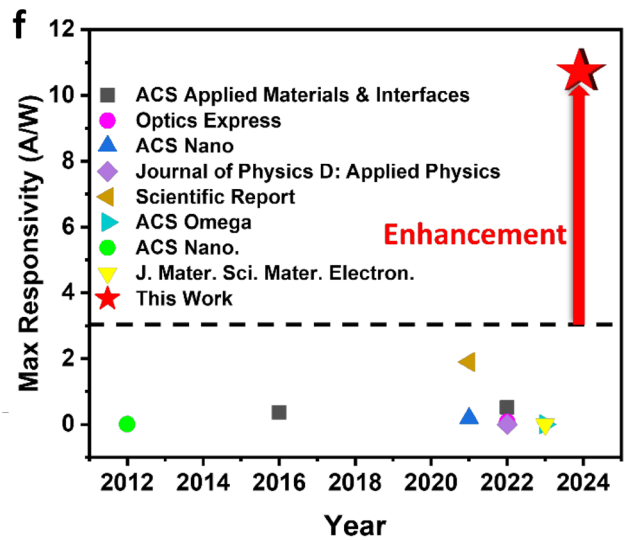
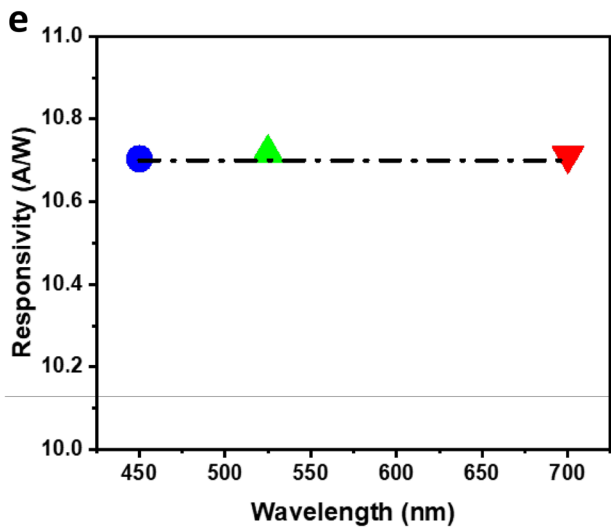
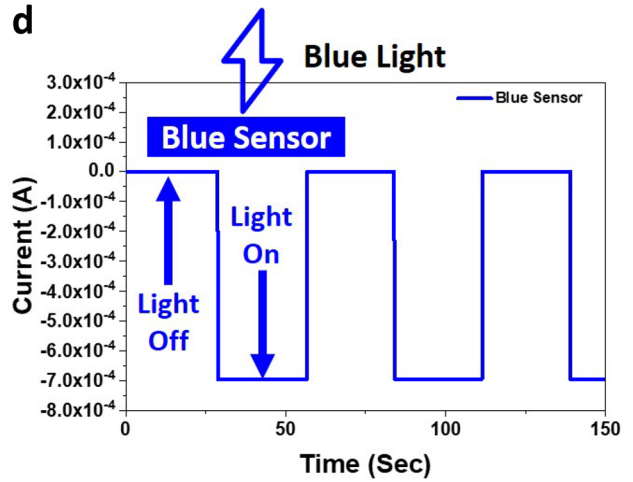
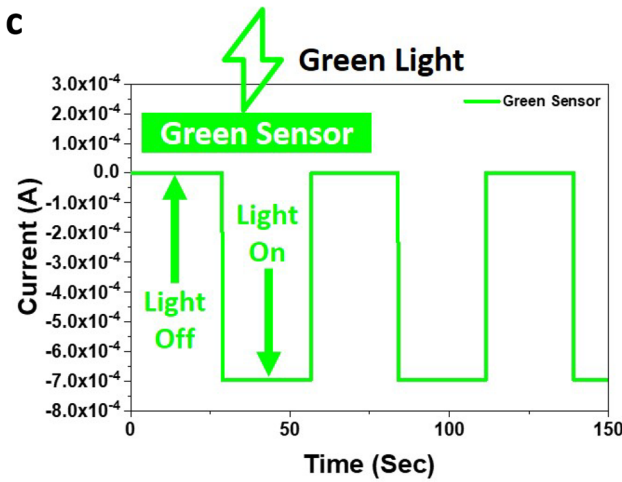
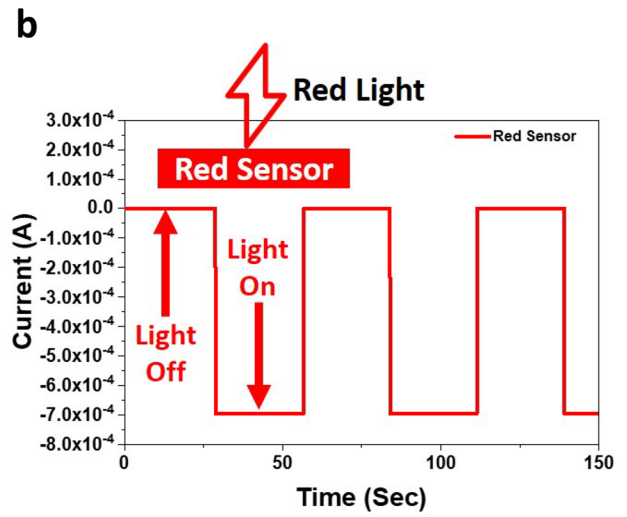
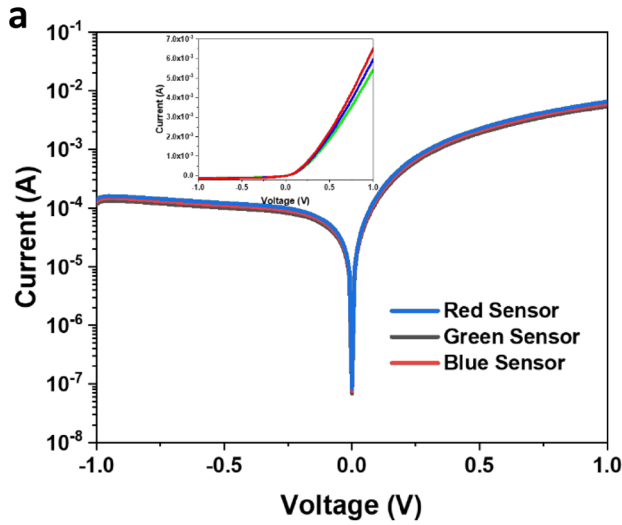


Fig. 4 AZO devices from in situ-doped interrupted flow ALD films with thicknesses of 54.6 nm (blue sensor), 65.8 nm (green sensor), and 91.7 nm (red sensor): **a** I–V curve of AZO/n-Si Schottky junction device in the dark and the inset of the log scale for the current; **b** 700-nm red light switching on–off current for the Schottky device with a 91.7 nm AZO film; **c** 525-nm green light switching on–off current for the Schottky device with a 65.8-nm AZO film; **d** 450-nm blue light switching on–off current for the Schottky device with a 54.6-nm AZO film; **e** responsivity of the three types of visible light sensors under illumination at their respective optimal detection wavelengths; and **f** comparison of the responsivity of the visible light sensors in this work with that of other light sensors [17, 46–53]

Table 1 presents a systematic collation of the results depicted in Fig. 4f, facilitating more intuitive observation and comparative analysis. Numerous investigations have been conducted to compare a variety of entities ranging from complex structures and partial two-dimensional materials to photodetectors employing identical AZO materials. Within this diverse spectrum of studies, the photodetector developed herein demonstrates superior photoresponsivity, achieving a remarkable figure of 10.7 AW^{-1} , which is several orders of magnitude greater than that of the comparative subjects. Additionally, the visible light detector devised in this research obviates the need for any voltage bias, enhancing a relatively simplistic design. This simplicity is promising because of its potential for integration with chemical identification techniques, such as colorimetry or fluorescence methods, enabling the detection of intensity variations in specific wavelength light sources. Consequently, this integration is anticipated to facilitate self-powering, rapid, cost-effective, and highly efficient detection.

The carrier concentrations from Hall measurements for the AZO films obtained at different precursor compositions in the ALD reactor are shown in Fig. 5. Optimization of the concentration ratio of the precursor at 1:7 for TMA/DEZ results in the best carrier concentration of $3 \times 10^{20} \text{ cm}^{-3}$ and a lower film resistivity of $5 \times 10^{-4} \Omega\text{-cm}$. This low resistivity confirms the effective control of aluminum doping in AZO through the in situ doping method, allowing AZO to function as an electrode for the photodetector and eliminating the need for additional

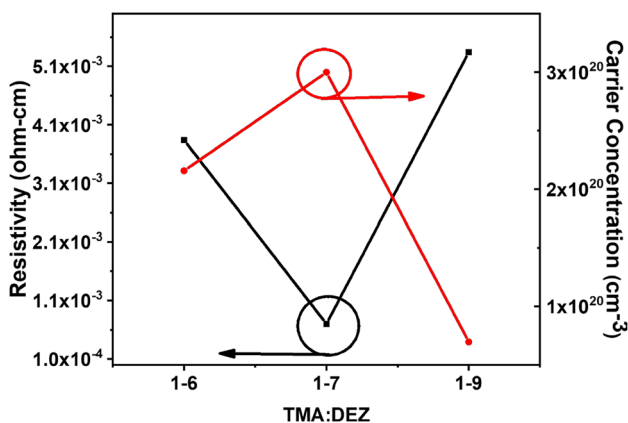
metal electrodes that could compromise the optical performance of the device. In contrast, a precursor ratio of 1:9 for TMA/DEZ results in a lower carrier concentration and higher film resistivity. The higher film resistivity is attributed to the lower Al doping in AZO, which yields a lower carrier concentration. In addition, a lower carrier concentration and a higher film resistivity were also observed at 1:6 for TMA/DEZ, which is attributed to the excess Al atoms not being able to fully replace the Zn atoms but rather easily forming Al_2O_3 to cause this phenomenon.

4 Conclusion

This work introduces a device with a controllable wavelength under visible light and a high responsivity utilizing heavily doped AZO thin films on n-type silicon. The AZO films are engineered via ALD using an interrupted flow and in situ doping method. The ability of the AZO films to control the thickness enables an antireflection coating at a specific wavelength through thin-film interference to facilitate optical absorption of the visible light sensor. Beyond serving as an antireflection coating at specific wavelengths, AZO films function as transparent electrodes and Schottky junctions form over n-type silicon to produce multifunctional AZO materials. This simplifies the device structure for enhancing the photoelectric conversion efficiency at specific wavelengths. The sensor exhibits ultrahigh responsivity, reaching 10.7 AW^{-1} , which is significantly superior to that of existing technologies. Consequently, this work demonstrates the potential of AZO as a multifunctional material for photodetector applications to provide advantages in optical (spectral/high optical absorbance in specific wavelengths), electrical (high conductivity), and fabrication aspects (accurately controlled thickness by ALD) for significant advancements in the field of high sensitivity photodetector applications, including biomedicine, communications, and environmental monitoring.

Table 1 Comparison of light detectors with different materials and device structures

Material and device structure	Photo responsivity (AW^{-1})	Bias voltage (V)
Al/n-type silicon with nanohole array [17]	0.25	0
AZO/n-type silicon [46]	0.128	2
AZO/TFB [47]	0.025	0
AZO/CuCrO ₂ [48]	0.001645	0
Ag nanodisk array on n-type silicon [49]	0.0915	0
ZnO/Perovskite/NiO [50]	0.55	0
Double organic bulk heterojunction [51]	0.2	0
Fe ₃ O ₄ /MoS ₂ [52]	0.0000101	0
MoS ₂ field-effect transistor [53]	0.008	40
AZO/n-type silicon (this work)	10.7	0

**Fig. 5** Carrier concentration and film resistivity for the AZO films obtained at different precursor compositions of 1:6, 1:7, and 1:9 for TMA/DEZ in the interrupted flow ALD reactor

Author contributions

Po-Hsien Tseng contributed to work plan, experimentation, data analysis, and manuscript writing; Yu-Sheng Lai contributed to manuscript writing, reviewing, and supervision; Cheng-Ming Huang contributed to Experimentation; Shang-Yu Tsai contributed to data analysis; Fu-Hsiang Ko contributed to manuscript writing and supervision.

Funding

Open Access funding enabled and organized by National Yang Ming Chiao Tung University. The authors are grateful to the National Science and Technology Council of Taiwan for financially supporting this research under contracts NSTC 112-2113-M-A49-025, NSTC 112-2119-M-002-032-MBK and NSTC 112-2119-M-492-002-MBK. This work was supported by the Higher Education Sprout Project of the National Yang Ming Chiao Tung University and Ministry of Education (MOE), Taiwan. We also thank the Taiwan Semiconductor Research Institute (TSRI), Hsinchu, for the device processing and characterization supported.

Data availability

The datasets used and analyzed during the current study are available from the corresponding author on reasonable request.

Declarations

Competing interests The authors declare that they have no known competing financial interests or personal relationships that could have appeared to influence the work reported in this paper.

Rights and permissions Springer Nature or its licensor (e.g., a society or other partner) holds exclusive rights to this article under a publishing agreement with the author(s) or other rights holder(s). Author self-archiving of the accepted manuscript version of this article is solely governed by the terms of such publishing agreement and applicable law.

Open Access This article is licensed under a Creative Commons Attribution 4.0 International License, which permits use, sharing, adaptation, distribution and reproduction in any medium or format, as long as you give appropriate credit to the original author(s) and the source, provide a link to the Creative Commons licence, and indicate if changes were made. The images or other third party material in this article are included in the article's Creative Commons licence, unless indicated otherwise in a credit line to the material. If material is not included in the article's Creative Commons licence and your intended use is

not permitted by statutory regulation or exceeds the permitted use, you will need to obtain permission directly from the copyright holder. To view a copy of this licence, visit <http://creativecommons.org/licenses/by/4.0/>.

References

- J. Shin, B. Jeong, J. Kim, V.B. Nam, Y. Yoon, J. Jung, S. Hong, H. Lee, H. Eom, J. Yeo, J. Choi, D. Lee, S.H. Ko, *Adv. Mater.* **32**, 1905527 (2020)
- J.D. Choi, M.Y. Kim, *ICT Express* **9**, 222 (2023)
- S.M. Majhi, A. Mirzaei, H.W. Kim, S.S. Kim, T.W. Kim, *Nano Energy* **79**, 105369 (2021)
- G. Korotcenkov, B.K. Cho, *Sens. Actuators, B Chem.* **244**, 182 (2017)
- Y. Gao, H. Ota, E.W. Schaler, K. Chen, A. Zhao, W. Gao, H.M. Fahad, Y. Leng, A. Zheng, F. Xiong, C. Zhang, L.-C. Tai, P. Zhao, R.S. Fearing, A. Javey, *Adv. Mater.* **29**, 1701985 (2017)
- L.-Q. Tao, K.-N. Zhang, H. Tian, Y. Liu, D.-Y. Wang, Y.-Q. Chen, Y. Yang, T.-L. Ren, *ACS Nano* **11**, 8790 (2017)
- K.E. Chang, C. Kim, T.J. Yoo, M.G. Kwon, S. Heo, S.-Y. Kim, Y. Hyun, J.I. Yoo, H.C. Ko, B.H. Lee, *Adv. Electron. Mater.* **5**, 1800957 (2019)
- S.R. Tamalampudi, G. Dushaq, N.S. Rajput, M. Chiesa, M.S. Rasras, *IEEE Electron Device Lett.* **43**, 2125 (2022)
- Z. Chunjiao, in *Intelligence computation and evolutionary computation*. ed. by Z. Du (Springer, Berlin Heidelberg, 2013), p.671
- C.M.D. Morais, D. Sadok, J. Kelner, J. Brazilian Comput. Soc. **25**, 4 (2019)
- N. Teranishi, H. Watanabe, T. Ueda, and N. Sengoku, in *2012 International Electron Devices Meeting 2012*, pp. 24.1.1.
- J. Cong, A. Khan, P. Hang, D. Yang, X. Yu, *ACS Appl. Electron. Mater.* **4**, 1715 (2022)
- Z. Yu, J. Cong, A. Khan, P. Hang, D. Yang, X. Yu, *Nanotechnology* **35**, 115703 (2024)
- J. Cong, A. Khan, P. Hang, L. Cheng, D. Yang, X. Yu, *Nanotechnology* **33**, 505201 (2022)
- A. Khan, R.R. Kumar, J. Cong, M. Imran, D. Yang, X. Yu, *Adv. Mater. Interfaces* **9**, 2100977 (2022)
- J. Cong, A. Khan, J. Li, Y. Wang, M. Xu, D. Yang, X. Yu, *ACS Appl. Electron. Mater.* **3**, 5048 (2021)
- K.-T. Lin, H.-L. Chen, Y.-S. Lai, Y.-M. Chi, T.-W. Chu, *ACS Appl. Mater. Interfaces* **8**, 6718 (2016)
- S. Zinatloo-Ajabshir, H. Mahmoudi-Moghaddam, M. Amiri, H. Akbari Javar, *J. Mater. Sci.: Mater. Electron.* **35**, 500 (2024)
- S. Jarollahi, G. Nabiyouni, Z. Sorinezami, A. Shabani, *J. Nanostruct.* **13**, 359 (2023)
- S. Zinatloo-Ajabshir, M. Salavati-Niasari, *J. Mol. Liq.* **216**, 545 (2016)
- S. Zinatloo-Ajabshir, M.S. Morassaei, M. Salavati-Niasari, *Compos. B Eng.* **167**, 643 (2019)
- G. Hosseinzadeh, S.M. Sajjadi, L. Mostafa, A. Yousefi, R.H. Vafaie, S. Zinatloo-Ajabshir, *Surfaces Interfaces* **42**, 103349 (2023)
- S. Zinatloo-Ajabshir, M. Salavati-Niasari, *Compos. B Eng.* **174**, 106930 (2019)
- S. Zinatloo-Ajabshir, M.H. Esfahani, C.A. Marjerrison, J. Greedan, M. Behzad, *Ceram. Int.* **49**, 37415 (2023)
- Q. Zhang, Y. Zhao, Z. Jia, Z. Qin, L. Chu, J. Yang, J. Zhang, W. Huang, X.A. Li, *Energies* **9**, 443 (2016)
- D.R. Sahu, S.-Y. Lin, J.-L. Huang, *Appl. Surf. Sci.* **252**, 7509 (2006)
- C. Wang, B. Hu, L. Chen, Y. Ye, *Opt. Laser Technol.* **153**, 108189 (2022)
- R. Yue, S.G. Ramaraj, H. Liu, D. Elamaran, V. Elamaran, V. Gupta, S. Arya, S. Verma, S. Satapathi, Y. Hayawaka, X. Liu, *J. Alloys Compounds* **918**, 165653 (2022)
- W. Wu, Z.L. Wang, *Nat. Rev. Mater.* **1**, 16031 (2016)
- C. Pan, J. Zhai, Z.L. Wang, *Chem. Rev.* **119**, 9303 (2019)
- R. Liu, Z.L. Wang, K. Fukuda, T. Someya, *Nat. Rev. Mater.* **7**, 870 (2022)
- Y.-C. Lee, J.-Y. Juang, *J. Eur. Ceram. Soc.* **42**, 3234 (2022)
- X. Wang, X. Huang, Z.M. Wong, A. Suwardi, Y. Zheng, F. Wei, S. Wang, T.L. Tan, G. Wu, Q. Zhu, H. Tanoto, K.S. Ong, S.-W. Yang, A.Q. Yan, J. Xu, *ACS Appl. Nano Mater.* **5**, 8631 (2022)
- M.H. Cho, C.H. Choi, J.K. Jeong, *ACS Appl. Mater. Interfaces* **14**, 18646 (2022)
- H. Liu, V. Avrutin, N. Izyumskaya, Ü. Özgür, H. Morkoç, *Superlatt. Microstruct.* **48**, 458 (2010)
- S. Peng, W. Wang, T. Yao, M. Guan, Z. Gan, J. Chu, L. Gai, *Int. J. Appl. Glas. Sci.* **14**, 133 (2023)
- S. Gao, X. Zhao, Q. Fu, T. Zhang, J. Zhu, F. Hou, J. Ni, C. Zhu, T. Li, Y. Wang, V. Murugadoss, G.A.M. Mersal, M.M. Ibrahim, Z.M. El-Bahy, M. Huang, Z. Guo, *J. Mater. Sci. Technol.* **126**, 152 (2022)
- M.R. Islam, M. Rahman, S.F.U. Farhad, J. Podder, *Surfaces and Interfaces* **16**, 120 (2019)
- V.H. Nguyen, J. Resende, D.T. Papanastasiou, N. Fontanals, C. Jiménez, D. Muñoz-Rojas, D. Bellet, *Nanoscale* **11**, 12097 (2019)
- Z. Zhang, Y. Guo, X. Wang, D. Li, F. Wang, S. Xie, *Adv. Func. Mater.* **24**, 835 (2014)
- D.K. Ghosh, S. Bose, G. Das, S. Mukhopadhyay, A. Sengupta, *J. Mater. Sci.: Mater. Electron.* **34**, 2189 (2023)

42. N.P. Poddar, S.K. Mukherjee, *J. Mater. Sci.: Mater. Electron.* **30**, 14269 (2019)
43. R. Bekkari, L. Laânab, B. Jaber, *J. Mater. Sci.: Mater. Electron.* **33**, 20353 (2022)
44. D.S. Bhachu, G. Sankar, I.P. Parkin, *Chem. Mater.* **24**, 4704 (2012)
45. J. He, Y. Hu, B. Zhang, Y. Cai, S. Wan, *J. Mater. Sci.: Mater. Electron.* **34**, 1752 (2023)
46. B.C. Şakar, Z. Orhan, F. Yıldırım, Ş Aydoğan, *J. Phys. D Appl. Phys.* **55**, 425107 (2022)
47. M.H. Tran, T.M.H. Nguyen, C.W. Bark, *ACS Omega* **8**, 35343 (2023)
48. M. Ahmadi, M. Abrari, M. Ghanaatshoar, *Sci. Rep.* **11**, 18694 (2021)
49. Z. Wu, Y. Zhai, C. Zhang, G. Zhang, Q. Wang, *Opt. Express* **30**, 25926 (2022)
50. W. Qarony, H.A. Khan, M.I. Hossain, M. Kozawa, A. Salleo, J.Y. Hardeberg, H. Fujiwara, Y.H. Tsang, D. Knipp, *ACS Appl. Mater. Interfaces.* **14**, 11645 (2022)
51. Z. Lan, F. Zhu, *ACS Nano* **15**, 13674 (2021)
52. S. Praisudan, P. Kathirvel, S.D.G. Ram, *J. Mater. Sci.: Mater. Electron.* **35**, 45 (2023)
53. Z. Yin, H. Li, H. Li, L. Jiang, Y. Shi, Y. Sun, G. Lu, Q. Zhang, X. Chen, H. Zhang, *ACS Nano* **6**, 74 (2012)

Publisher's Note Springer Nature remains neutral with regard to jurisdictional claims in published maps and institutional affiliations.